JOURNAL OF COMPUTATIONAL PHYSICS 97, 489–515 (1991)

Nonlinear Oscillations of Inviscid Free Drops*

T. W. PATZEK,† R. E. BENNER, JR,‡
O. A. BASARAN,§ AND L. E. SCRIVEN

Department of Chemical Engineering and Materials Science, University of Minnesota, Minneapolis, Minnesota 55455

Received May 10, 1990; revised January 27, 1991

Inviscid oscillations of free liquid drops are analyzed by solving Bernoulli's equation for the free surface shape and Laplace's equation for the velocity potential field. The means are: (a) Galerkin's weighted residual method which converts the governing equations into a large system of nonlinear, time-dependent ordinary differential equations; (b) an implicit predictor-corrector method for time integration which automatically adjusts time steps; and (c) Newton's method which solves the large system of nonlinear algebraic equations that results from time discretization. Results presented include sequences of drop shapes, pressure distributions, particle paths, and evolution with time of kinetic and surface energies. Accuracy is attested by virtual constancy of drop volume and total energy *and* smallness of mass and momentum fluxes across drop surfaces. Dynamic response to small amplitude disturbances agrees with linear theory. Large-amplitude oscillations are compared to the predictions by the marker-and-cell method and second-order perturbation theory. Mode interactions and frequency shifts are analyzed by Fourier power spectra and lend further insight into the nature of the oscillations.

1. INTRODUCTION

Oscillating drops, the subject of this paper, are central to diverse processes in industry and nature, e.g., various mass transfer operations in chemical engineering [1], containerless processing in low-gravity [2, 3], and cloud physics [4], and have been the focus of many theoretical analyses to date. All such analyses start

* Research sponsored by the NASA Fund for Independent Research, the University of Minnesota Computer Center, and the Office of Basic Energy Sciences, U.S. Department of Energy under Contract DE-AC05-84OR21400 with Martin Marietta Energy Systems, Inc. Correspondence regarding this paper may be addressed to either T. W. Patzek or O. A. Basaran.

† Presently at: Department of Materials Science and Mineral Engineering, University of California at Berkeley, Berkeley, CA 94720.

‡ Presently at: Sandia National Laboratories, Albuquerque, NM 87185.

§ Presently at: Chemical Technology Division, Oak Ridge National Laboratory, Oak Ridge, TN 37831.

0021-9991/91 $3.00

from the statements of mass and momentum conservation, i.e., the continuity and Navier–Stokes equations:

$$\tilde{\nabla} \cdot \tilde{\mathbf{v}} = 0 \tag{1}$$

$$\frac{\rho L^2}{\mu t^*}\left(\frac{\partial \tilde{\mathbf{v}}}{\partial \tilde{t}} + \frac{A}{L}\tilde{\mathbf{v}} \cdot \tilde{\nabla}\tilde{\mathbf{v}}\right) = -\frac{p^* L t^*}{\mu A}\tilde{\nabla}\tilde{p} + \tilde{\nabla} \cdot \tilde{\tau}. \tag{2}$$

Here ρ is the density, L is the wavelength along the interface (i.e., a length scale that is proportional to the drop radius), and μ is the viscosity. Thus $\rho L^2/\mu t^*$ is the ratio of the time scale for vorticity diffusion to the time scale for fluid motion t^*. The length scale A is a measure of the deformation of the interface. Finally, variables with tildes over them are dimensionless: velocity $\tilde{\mathbf{v}}$ is measured in units of A/t^*, time $\tilde{t}$ is measured in units of t^*, gradient operator $\tilde{\nabla}$ is measured in units of L^{-1}, pressure $\tilde{p}$ is measured in units of some characteristic pressure p^*, and viscous stress $\tilde{\tau}$ is measured in units of $\mu(A/t^*)/L$. Dramatically different flow regimes result as $\rho L^2/\mu t^*$ and A/L vary between 0 and ∞, as shown in Fig. 1.

Infinitesimal amplitude ($A/L \to 0$) oscillations of a free, inviscid ($\rho L^2/\mu t^* \to \infty$), and incompressible drop were first analyzed by Rayleigh [5]. He expressed the fundamental modes of oscillation in terms of Legendre polynomials, P_n,

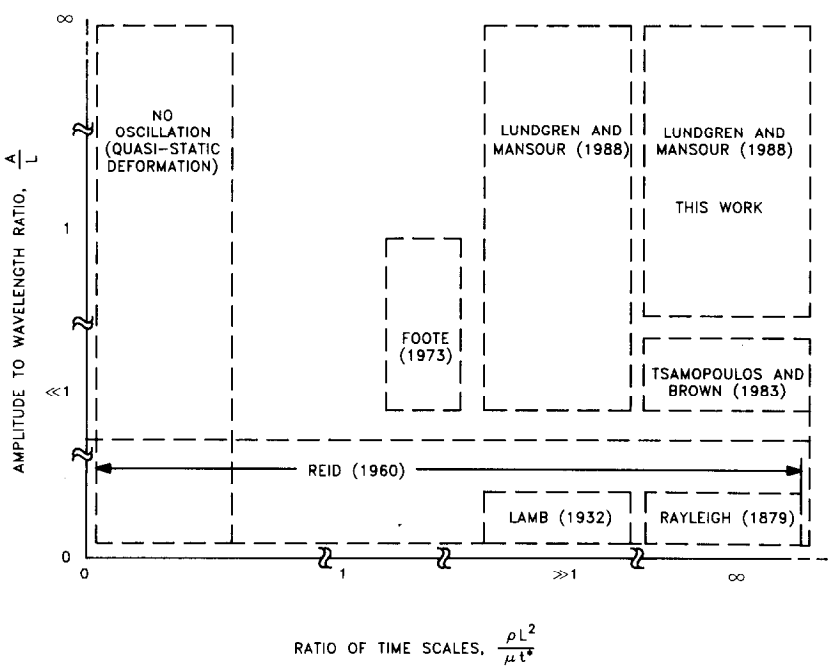

FIG 1. A liquid drop oscillating in a vacuum or a gas of negligible density and viscosity: previous work and opportunities for analysis.

$n = 2, 3, 4, \ldots$, and calculated the corresponding frequencies. *Small* amplitude ($A/L \ll 1$) oscillations were later analyzed by Tsamopoulos and Brown [6] with a Poincaré–Linstedt expansion technique that extends Rayleigh's analysis to second order for certain combinations of mode coupling and allows solutions for *periodic* motions resulting from initially second, third, and fourth harmonic oscillations, i.e., $n = 2$, 3, and 4. *Large* amplitude ($A/L = \mathcal{O}(1)$), high-frequency ($n \geq 4$) drop oscillations were recently studied by Lundgren and Mansour [7], who employed a boundary integral method. Lundgren and Mansour [7] also extended their method to account for the effects of "small" viscosity on drop oscillations. However, by its nature, the boundary integral method cannot model drop oscillations when viscous effects are "large," as shown below.

The perturbation analysis of Tsamopoulos and Brown [6] predicts a decrease in frequency with increasing amplitude of oscillation. The predicted frequency shift of the second mode agrees with experiments [8] and other calculations [9–11]. Trinh and Wang [8] performed experiments on acoustically levitated drops of low viscosity that were nearly neutrally buoyant in the surrounding liquid. Foote [9] simulated the moderate amplitude, axisymmetric oscillations of a low viscosity drop by the marker-and-cell (MAC) method. Alonso [10] and Alonso *et al.* [11] simulated axisymmetric oscillations of highly viscous, charged drops undergoing large-amplitude, second-harmonic oscillations by the MAC method.

The MAC method is complicated and requires computations on a pair of finite difference grids, one fixed and one moving [12]. Nevertheless, Harlow *et al.* [13] and Nix and Strottman [14] have extended the MAC analysis to fluid motions in three dimensions. Because of its complexity, the MAC method cannot compete in computational efficiency with finite element [15] or spectral [16] methods.

Drop oscillations, and also other free surface flows, can be tackled with either of two standard approaches: (a) the *domain differential* (DD) method that entails solving Eqs. (1)–(2) **within the drop volume** with appropriate boundary conditions along the drop surface or (b) the *boundary integral* (BI) method that requires solution of an associated integral equation **on the drop surface alone**. As shown in Fig. 2, an often more cumbersome DD approach is feasible everywhere in the (A/L, $\rho L^2/\mu t^*$) space, whereas a simpler BI formulation is limited to *steady, quasi-steady, or transient Stokes flows* and to *inviscid, irrotational flows*. This is because the boundary integral equations can be derived only when Eqs. (1)–(2) are linear, so that a Green's function or a fundamental solution can be found (cf. [17, 18]).

In this paper, we focus on the large amplitude oscillations of inviscid drops, but eventually want to include viscous effects of any magnitude. With this in mind, we choose the DD approach and solve Laplace's equation for the velocity potential field in the drop volume, subject to appropriate boundary conditions along the drop surface. This approach is simple, but the velocity potential field must be calculated *a posteriori* from the gradient of the potential field. Finite element methods are well suited for such calculations and the attained accuracy is remarkable because of the super-convergence properties of the potential approximation [19]. The BI approach, equally feasible here, but unfit to model viscous effects

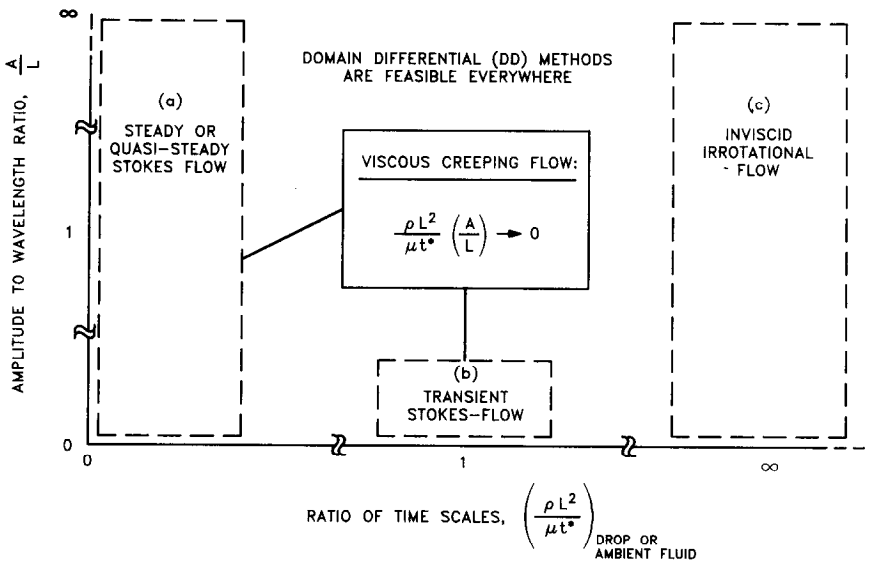

FIG. 2. Regions of applicability of boundary integral methods. Equations (1) and (2) are linear in regions (a), (b), and (c), permitting the determination of a fundamental solution or a Green's function on which the BI methods rely.

of any magnitude, would involve solution of an associated integral equation for the velocity potential field and/or its gradient on the drop surface alone.

Here, we present a simple, flexible and inexpensive DD method for studying large amplitude oscillations of inviscid axisymmetric free drops. The method features simultaneous solution of mass and momentum conservation equations for the velocity potential field and free surface location. The means are Galerkin's weighted residual method, with the velocity potential in axisymmetric drops represented by biquadratic finite element basis functions on a tessellation that deforms in proportion to the free surface. The Galerkin/finite element method converts the governing equations into a large system of nonlinear, time-dependent ordinary differential equations. The transient problem is solved by means of an implicit predictor-corrector method which automatically adjusts time steps [15]. The large system of nonlinear algebraic equations that results from time discretization is then solved by Newton's method. The present method grew out of methods developed for simulation of steady [20, 21] and unsteady [22] viscous free surface film flows.

The BI method has been applied to diverse problems of inviscid flow in which the interface shapes can be quite complex, as in the breaking of water waves [23, 24] and the Rayleigh–Taylor instability [25]. A major advantage of BI methods is that they reduce the dimension of the problem by one. However, Hume *et al.* [26] showed that algorithms based on the DD and BI methods for solving potential problems based on Laplace's equation have comparable accuracy at the same computational cost if the region inside which the equations of the DD method are to

be solved is finite in size, as is the case for an oscillating drop. As an aside, Lundgren and Mansour [7] used (a) an explicit time integrator with fixed time-step size in their analysis of inviscid oscillations by the BI method and (b) artificial dissipation to suppress numerical instabilities. The implicit predictor-corrector scheme used here requires no such suppression and allows time-step sizes that are one to two orders of magnitude larger than those possible with the explicit time integrator used by Lundgren and Mansour [7].

The Galerkin method with finite element basis functions as applied in this paper is an example of "the method of lines" and is readily extended to more complex cases. Elsewhere, the effect of rotation is highlighted in analysis of a simple, two-dimensional system, the inviscid oscillations of rotating cylindrical drops [27, 28]. When the drop rotates, the free surface Bernoulli equation, which governs the drop shape, becomes an integro-differential equation. The effect of net surface charge or an imposed electric field upon an oscillating axisymmetric inviscid drop has also beeen studied [29, 30]. In these cases of electrified drop oscillation, Laplace's equation for electric potential outside the drop and the constraint of net surface charge are solved simultaneously with Laplace's equation for velocity potential inside the drop and Bernoulli's equation for free surface shape. These two situations can of course be analyzed just as well by means of the BI method.

Both the field and BI methods of modeling inviscid drop oscillations can be readily extended to include viscous effects that are confined to thin surface layers, as shown by Lundgren and Mansour [7]. An important example of such flows is

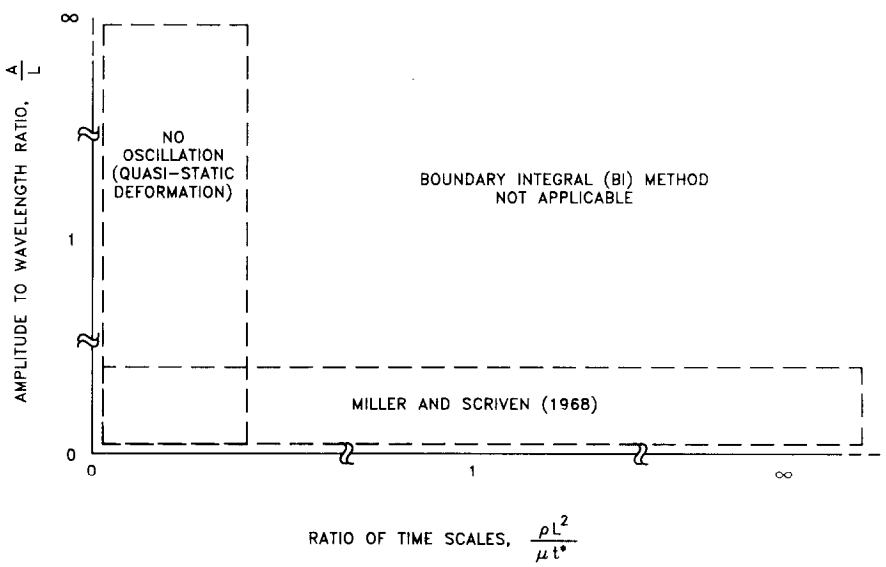

FIG. 3. A viscous liquid drop oscillating in another viscous liquid: previous work and opportunities for analysis.

an oscillating liquid drop which is srurrounded by a dynamically inactive environment—i.e., the environment surrounding the drop is either a vacuum or a gas of negligible density and viscosity—and in the absence of any solid boundaries, as occurs in containerless processing in low gravity [2, 3]. However, there are many applications, such as the diverse mass transfer operations of chemical engineering, in which the environment surrounding the drop is far from inactive, e.g., as in solvent extraction, where the fluid surrounding the liquid drops is another viscous liquid and solid boundaries abound. As shown by Miller and Scriven [31] and pointed out by Lundgren and Mansour [7], the effect of viscosity is much greater at the interface of an oscillating drop in liquid–liquid systems and cannot be accounted for by the BI methods (cf. Fig. 3).

The theory and formulation of the governing equations and their Galerkin/finite element weighted residuals are presented in Sections 2 and 3. Computer-aided analysis is discussed in Section 4. Results for moderate and large amplitude oscillations of axisymmetric drops are presented and compared to previous investigations in Section 5.

2. Theory of Drop Motion

The system is a drop of inviscid, incompressible liquid of volume V bounded by free surface $S(t)$ that separates the liquid from a fluid that exerts uniform pressure and negligible viscous drag on the drop. The fluid motion satisfies equations of mass and linear momentum conservation (cf. Eqs. (1)–(2)),

$$\nabla \cdot \dot{\mathbf{x}} = 0 \qquad \text{in } V \tag{3}$$

and

$$\rho \ddot{\mathbf{x}} + \nabla p = \mathbf{0} \qquad \text{in } V, \tag{4}$$

respectively, subject to the kinematic

$$\mathbf{n} \cdot (\dot{\mathbf{x}} - \dot{\mathbf{x}}_S) = 0 \qquad \text{on } S(t) \tag{5}$$

and normal stress

$$p(\mathbf{x}, t) = -2H\sigma \qquad \text{on } S(t) \tag{6}$$

boundary conditions. Here $\mathbf{x}$ and $\mathbf{x}_S$ are the coordinates of points located in V and on $S(t)$, respectively; ρ is density, σ surface tension, t time,

$$\dot{(\ )} = \frac{\partial}{\partial t} + \dot{\mathbf{x}} \cdot \nabla(\ ), \tag{7}$$

the convective derivative, H the local mean curvature of $S(t)$, given by the surface divergence ∇_S of the outward unit normal $\mathbf{n}$ [32],

$$H(\mathbf{x}, t) = -\tfrac{1}{2}\nabla_S \cdot \mathbf{n}, \tag{8}$$

and constant pressure outside the drop is set to zero (cf. Eq. (6)).

We seek oscillatory solutions of the nonlinear, time-dependent partial differential equations (3)–(4) and boundary conditions (5)–(6). The approach to a limit cycle (drop motion governed by one frequency of oscillation), quasiperiodic oscillation (drop motion governed by several frequencies of oscillation), or breakup is determined by the initial conditions

$$S(0) = S_0, \tag{9}$$

$$\dot{\mathbf{x}}(\mathbf{x}, 0) = \dot{\mathbf{x}}_0(\mathbf{x}). \tag{10}$$

The modeling of initial conditions is important. A simulation should be started close to a steady oscillation, if possible, because time truncation error accumulates and erodes the accuracy of solutions at large times. Initial conditions that are physically realistic correspond to a drop that is (a) released from a static deformation, (b) set in motion by a pressure impulse, or (c) released from a steady acoustic drive (see Section 5).

Incompressible inviscid fluid motion is irrotational. A velocity potential $\phi(\mathbf{x}, t)$ is defined as

$$\dot{\mathbf{x}} = \nabla\phi \qquad \text{in } V. \tag{11}$$

Equations (3) and (11) become Laplace's equation for velocity potential,

$$\nabla^2\phi = 0 \qquad \text{in } V. \tag{12}$$

Equations (4) and (11) evaluated at $S(t)$ become Bernoulli's equation for free surface shape,

$$\frac{\partial\phi}{\partial t} + \frac{1}{2}(\nabla\phi)^2 - \frac{\sigma}{\rho}2H = 0 \qquad \text{on } S(t), \tag{13}$$

where the normal stress condition (6) has been used to substitute for p. Therefore, motions of inviscid, incompressible drops are calculated by solving Laplace's equation (12) in spatial domain V which evolves according to the nonlinear, time-dependent Bernoulli equation (13) imposed at free surface $S(t)$. Initial conditions upon drop shape, Eq. (9), and velocity potential,

$$\phi(\mathbf{x}, 0) = \phi_0(\mathbf{x}), \tag{14}$$

derived from Eq. (10), are discussed in Section 5.

The preceding equations can be expressed in terms of $\tilde{\mathbf{x}} \equiv \mathbf{x}/R$, $\tilde{t} \equiv v_{\min} t$, and $\tilde{\phi} \equiv \phi/(v_{\min} R^2)$, which are measured in units of R, the radius of the unperturbed drop, and $v_{\min} = (8\sigma/\rho R^3)^{1/2}$, the lowest angular frequency of small amplitude oscillations of inviscid spherical drops, corresponding to the second harmonic [5, 33, 34]. The equations that follow are dimensionless, with tildes suppressed for simplicity.

3. Computer-Aided Finite Element Analysis

Conservation equations (12) and (13) are solved here by the Galerkin/finite element method. In spherical polar coordinates (r, θ, Φ) the drop surface $f(\theta, t)$ and the field of outward pointing unit normals to the drop surface are, respectively,

$$\mathbf{x} = f(\theta, t)\, \mathbf{e}_r(\theta, \Phi) \tag{15}$$

$$\mathbf{n} = \frac{f\mathbf{e}_r - f_\theta \mathbf{e}_\theta}{(f^2 + f_\theta^2)^{1/2}}, \tag{16}$$

where $(\mathbf{e}_r, \mathbf{e}_\theta, \mathbf{e}_\Phi)$ are the unit vectors in the coordinate directions and $f_\theta \equiv \partial f/\partial\theta$.

The weak forms of Eqs. (12) and (13) are

$$\int_V \psi^i \nabla^2 \phi \, dV = 0, \qquad i = 1, ..., N, \tag{17}$$

$$\int_{S(t)} \left[\frac{\partial \phi}{\partial t} + \frac{1}{2}(\nabla\phi)^2 - \frac{1}{8}(2H) \right] \mathbf{e}_r \cdot \mathbf{n} \psi^j \, dS = 0, \qquad j = 1, ..., N_B. \tag{18}$$

Here N is the number of finite element basis functions ψ^i used in representing the velocity potential,

$$\phi(r, \theta, t) = \sum_{i=1}^{N} \beta_i(t)\, \psi^i(r, \theta). \tag{19}$$

The free surface is represented in a set of basis functions ψ^j, that is a subset of the set of basis functions ψ^i (see below),

$$f(\theta, t) = \sum_{j=1}^{N_B} \alpha_j(t)\, \psi^j(\theta). \tag{20}$$

The α_j and β_i are the unknown coefficients.

Green's theorem applied to Eq. (17) gives the Galerkin weighted residuals of Laplace's equation:

$$R_i \equiv \int_V \nabla\phi \cdot \nabla\psi^i \, dV - \int_{S(t)} \psi^i \mathbf{n} \cdot \nabla\phi \, dS = 0, \qquad i = 1, ..., N. \tag{21}$$

The surface divergence theorem [32],

$$-\int_S 2H(\psi^j \mathbf{e}_r)\cdot\mathbf{n}\, dS = \int_S \nabla_S\cdot(\psi^j\mathbf{e}_r)\, dS, \tag{22}$$

applied to the curvature term in (18) gives the Galerkin weighted residuals of the free surface Bernoulli equation:

$$R_j^* \equiv \int_{S(t)} \left\{\left[\frac{\partial\phi}{\partial t}+\frac{1}{2}(\nabla\phi)^2\right]\psi^j\mathbf{e}_r\cdot\mathbf{n}+\frac{1}{8}\nabla_S\cdot(\psi^j\mathbf{e}_r)\right\} dS = 0, \qquad j=1, ..., N_B. \tag{23}$$

Weighting factor $\psi^j\mathbf{e}_r\cdot\mathbf{n}$ chosen in Eq. (18) expedites use of the surface divergence theorem. For an axisymmetric surface [35],

$$\nabla_S\cdot(\psi^j\mathbf{e}_r)=\frac{f_\theta\psi^j_\theta+f\psi^j}{f^2+f_\theta^2}+\frac{\psi^j}{f}. \tag{24}$$

Here $\psi^j_\theta \equiv d\psi^j/d\theta$. Equations (21) and (23)–(24) require continuity of the basis functions that represent ϕ and f [36]; thus we choose the admissible C^0 biquadratic basis functions $\psi^i(r,\theta)$ and quadratic basis functions $\psi^j(\theta)$.

The drop folume $V=\{(\theta, r): 0\leqslant\theta\leqslant\pi,\ 0\leqslant r\leqslant f(\theta,t)\}$ is partitioned or tessellated into a set of $N_\theta\times N_r$ quadrilateral elements (cf. Fig. 4). The elements are bordered by the *fixed spines*,

$$\theta_{2i-1}=\frac{(i-1)\pi}{N_\theta}, \qquad i=1, ..., N_\theta+1, \tag{25}$$

and by the *curves*,

$$r_{2j-1}(\theta,t)=w_{2j-1}f(\theta,t), \qquad w_{2j-1}=(j-1)/N_r, \qquad j=1, ..., N_r+1, \tag{26}$$

which move proportionally to the free surface along the spines. In this paper, the spines are uniformly spaced coordinate lines and the weights w are unbiased, though in general they need not be so (cf. [21]). Equations (25) and (26) prescribe the positions of just the vertex-nodes of the elements. Mid-side and mid-element nodes are located by requiring mid-element spines and the weights to satisfy

$$\theta_{2i}=\frac{\theta_{2i-1}+\theta_{2i+1}}{2}, \qquad i=1, ..., N_\theta \tag{27}$$

$$w_{2j}=\frac{w_{2j-1}+w_{2j+1}}{2}, \qquad j=1, ..., N_r. \tag{28}$$

Each curvilinear element is mapped onto the unit square with coordinates (ξ,η), $0\leqslant\xi,\ \eta\leqslant 1$, by the isoparametric transformation [36]. On the unit square, nine biquadratic basis functions are defined in the standard way [36]. The basis

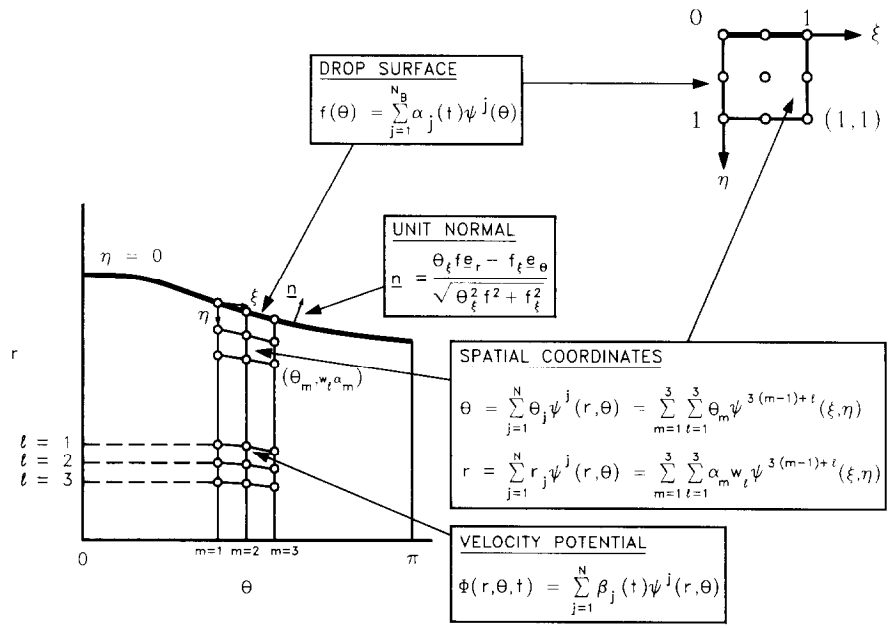

FIG. 4. Spatial and isoparametric finite elements.

functions have global numbers $i = 1, ..., N$, where $N \equiv (2N_\theta + 1) \times (2N_r + 1)$. Within an element the basis functions also have local numbers that correspond to nodal numbering in the mapped (ξ, η)-domain; cf. Fig. 4.

The free surface is interpolated globally and locally, respectively, as

$$f(\theta, t) = \sum_{j=1}^{N_B} \alpha_j(t)\,\psi^j[\theta(\xi, \eta = 0), r(\xi, \eta = 0)]$$
$$= \sum_{m=1}^{3} \alpha_m(t)\,\psi^{3m-2}(\xi, 0), \tag{29}$$

because the free surface maps onto the $\eta = 0$ edge of the (ξ, η)-domain. At the free surface, the set of biquadratic basis functions reduces to the standard set of three one-dimensional, quadratic basis functions, $\psi^{3m-2}(\xi, 0)$, $m = 1, ..., 3$, that represent free surface location.

Spatial coordinates (r, θ) are interpolated as (see Fig. 4)

$$\theta(\xi, \eta) = \sum_{j=1}^{N} \theta_j \psi^j(\xi, \eta) = \sum_{m=1}^{3}\sum_{l=1}^{3} \theta_m \psi^{l+3(m-1)}(\xi, \eta), \tag{30}$$

$$r(\xi, \eta, t) = \sum_{j=1}^{N} r_j(t)\,\psi^j(\xi, \eta) = \sum_{m=1}^{3}\sum_{l=1}^{3} \alpha_m(t)\,w_l \psi^{l+3(m-1)}(\xi, \eta). \tag{31}$$

Here $\{\theta_j, r_j(t)\}$ are the coordinates of the nodes, each belonging to spine θ_m—Eq. (25)—and having height w_l—Eq. (26)—in proportion to the corresponding free surface coefficient $\alpha_m(t)$. Equation (31) is also used to compute derivatives with respect to free surface location:

$$\frac{\partial r(\cdot)}{\partial \alpha_m} = \sum_{l=1}^{3} w_l \psi_{(\cdot)}^{3(m-1)+l}(\xi, \eta). \tag{32}$$

In Eq. (32), $r_{(\cdot)}$ stands for r, r_ξ, and $r_\eta, \psi_{(\cdot)}$ stands for ψ, ψ_ξ, and ψ_η, and $r_\xi \equiv \partial r/\partial \xi$, etc. Equation (32) makes plain that $\partial r/\partial \alpha_m$, $\partial r_\xi/\partial \alpha_m$, and $\partial r_\eta/\partial \alpha_m$ have the same values when evaluated at the same isoparametric coordinate in all elements of a row in the computational domain, the rectilinear domain obtained by retaining the adjacency structure of the elements in the physical domain but replacing each curvilinear element by the standard unit square from the (ξ, η)-domain. Equation (32) is evaluated at fixed Gauss points [36] in the isoparametric domain and needs to be calculated only once for a given set of weights $\{w_l\}$. This computational saving was not incorporated into their pioneering works by Saito and Scriven [20] and Kistler and Scriven [21].

Spatial derivatives are transformed to the isoparametric domain with the Jacobian $J \equiv \partial(\theta, r)/\partial(\xi, \eta)$. When spines of constant θ are used, θ is independent of η, and (see, e.g., [22])

$$J = \theta_\xi r_\eta. \tag{33}$$

Then,

$$\frac{\partial}{\partial \theta}(\ ) = \frac{1}{\theta_\xi}\left[\frac{\partial}{\partial \xi}(\ ) - \frac{r_\xi}{r_\eta}\frac{\partial}{\partial \eta}(\ )\right], \tag{34}$$

$$\frac{\partial}{\partial r}(\ ) = \frac{1}{r_\eta}\frac{\partial}{\partial \eta}(\ ). \tag{35}$$

Equation (34) simplifies further in the cases of free surface derivatives, e.g.,

$$\frac{\partial f}{\partial \theta} = \frac{f_\xi}{\theta_\xi}. \tag{36}$$

Time derivatives are also expressed in terms of derivatives $\mathring{\phi}$ and $\mathring{f}$ at fixed isoparametric coordinates, e.g., at nodes or Gauss points [15],

$$\frac{\partial \phi}{\partial t} = \mathring{\phi} - \mathring{f}\frac{\partial \phi}{\partial r} = \mathring{\phi} - \mathring{f}\frac{\phi_\eta}{r_\eta}, \qquad r = f, \eta = 0. \tag{37}$$

The relations developed above can be used to transform residuals (21) and (23)

to the isoparametric form. The kinematic condition (5) is used to evaluate the boundary term in Eq. (21),

$$\nabla\phi \cdot \mathbf{n} = \mathring{f}\mathbf{e}_r \cdot \mathbf{n} = \frac{f\mathring{f}}{\sqrt{f^2 + f_\xi^2/\theta_\xi^2}}. \tag{38}$$

With $dV = -r^2 \sin\theta\theta_\xi r_\eta \, d\xi \, d\eta \, d\Phi$, $dS = f \sin\theta \sqrt{f^2 + f_\xi^2/\theta_\xi^2}\theta_\xi \, d\xi \, d\Phi$ and integration over Φ, $0 \leqslant \Phi \leqslant 2\pi$, Eqs. (21) and (23) become

$$\begin{aligned} R_i = {} & \theta_\xi \int_0^1 \int_0^1 \frac{\phi_\eta}{r_\eta} \psi_\eta^i r^2 \sin\theta \, d\xi \, d\eta \\ & + \frac{1}{\theta_\xi} \int_0^1 \int_0^1 \left(\phi_\xi - \frac{r_\xi}{r_\eta}\phi_\eta\right)\left(\psi_\xi^i - \frac{r_\xi}{r_\eta}\psi_\eta^i\right) r_\eta \sin\theta \, d\xi \, d\eta \\ & + \theta_\xi \int_0^1 \mathring{f} f^2 \psi^i \sin\theta \, d\xi, \qquad i = 1, \ldots, N, \end{aligned} \tag{39}$$

$$\begin{aligned} R_j^* = {} & \theta_\xi \int_0^1 \left[\mathring{\phi} - \mathring{f}\frac{\phi_\eta}{r_\eta} + \frac{1}{2}\left(\frac{\phi_\eta}{r_\eta}\right)^2 + \frac{1}{2}\frac{1}{\theta_\xi^2 f^2}\left(\phi_\xi - \frac{r_\xi}{r_\eta}\phi_\eta\right)^2\right] \psi^j f^2 \sin\theta \, d\xi \\ & + \frac{1}{8}\int_0^1 \frac{f f_\xi \psi_\xi^j + \psi^j(2\theta_\xi^2 f^2 + f_\xi^2)}{\sqrt{\theta_\xi^2 f^2 + f_\xi^2}} \sin\theta \, d\xi = 0, \qquad j = 1, \ldots, N_B. \end{aligned} \tag{40}$$

Three by three-point and three-point Gaussian quadrature rules are used here to evaluate the surface and line integrals in Eqs. (39)–(40) [36].

4. Method of Solving the Transient Problem

The Galerkin/finite element weighted redisduals are a set of $(2N_\theta + 1)(2N_r + 2)$ nonlinear ordinary differential equations in time and can be expressed as

$$\begin{aligned} R_i(\boldsymbol{\alpha}, \boldsymbol{\beta}, \mathring{\boldsymbol{\alpha}}) &= 0, \qquad i = 1, \ldots, N, \\ R_j^*(\boldsymbol{\alpha}, \boldsymbol{\beta}, \mathring{\boldsymbol{\alpha}}, \mathring{\boldsymbol{\beta}}) &= 0, \qquad j = 1, \ldots, N_B. \end{aligned} \tag{41}$$

Time derivatives are discretized at the pth time step, $\Delta t_p = t_p - t_{p-1}$, by either first-order backward-differences or second-order trapezoid rule,

$$\begin{aligned} \mathring{\boldsymbol{\alpha}}(t_p) &= c_1[\boldsymbol{\alpha}(t_p) - \boldsymbol{\alpha}(t_{p-1})]/\Delta t_p + c_2\mathring{\boldsymbol{\alpha}}(t_{p-1}), \\ \mathring{\boldsymbol{\beta}}(t_p) &= c_1[\boldsymbol{\beta}(t_p) - \boldsymbol{\beta}(t_{p-1})]/\Delta t_p + c_2\mathring{\boldsymbol{\beta}}(t_{p-1}). \end{aligned} \tag{42}$$

Here $c_1 = 1$, $c_2 = 0$ for backward-differences, $c_1 = 2$, $c_2 = -1$ for trapezoid rule, and $\boldsymbol{\alpha}(t_{p-1})$, $\mathring{\boldsymbol{\alpha}}(t_{p-1})$, etc. are known from the previous time step.

With time discretization (42) in place, Eqs. (41) are solved by Newton iteration. Initial conditions (9) and (14) specified need not be harmonic, i.e., satisfy $\nabla^2\phi = 0$

exactly. Four backward-difference time steps with fixed Δt_p provide necessary smoothing [37] before the trapezoid rule is used. A first-order forward difference predictor,

$$\begin{aligned}\boldsymbol{\alpha}(t_{p+1}) &= \boldsymbol{\alpha}(t_p) + \dot{\boldsymbol{\alpha}}(t_p)\,\Delta t_{p+1},\\ \boldsymbol{\beta}(t_{p+1}) &= \boldsymbol{\beta}(t_p) + \dot{\boldsymbol{\beta}}(t_p)\,\Delta t_{p+1}\end{aligned} \tag{43}$$

is used with the backward-difference method. A second-order Adams–Bashforth predictor,

$$\begin{aligned}\boldsymbol{\alpha}(t_{p+1}) &= \boldsymbol{\alpha}(t_p) + \frac{\Delta t_{p+1}}{2}\left[\left(2+\frac{\Delta t_{p+1}}{\Delta t_p}\right)\dot{\boldsymbol{\alpha}}(t_p) - \frac{\Delta t_{p+1}}{\Delta t_p}\,\dot{\boldsymbol{\alpha}}(t_{p-1})\right]\\ \boldsymbol{\beta}(t_{p+1}) &= \boldsymbol{\beta}(t_p) + \frac{\Delta t_{p+1}}{2}\left[\left(2+\frac{\Delta t_{p+1}}{\Delta t_p}\right)\dot{\boldsymbol{\beta}}(t_p) - \frac{\Delta t_{p+1}}{\Delta t_p}\,\dot{\boldsymbol{\beta}}(t_{p-1})\right]\end{aligned} \tag{44}$$

is used with the trapezoid rule. The L_∞ norm of the correction provided by Newton iteration, $\|d_{p+1}\|_\infty$, is an estimate of the local time truncation error of the trapezoid rule [15]. The time step is chosen adaptively by requiring the norm of time truncation error at the next time step to be equal to a prescribed value, ε [15],

$$\Delta t_{p+1} = \Delta t_p(\varepsilon/\|d_{p+1}\|_\infty)^{1/3}. \tag{45}$$

Relative error of 0.1% per time step, $\varepsilon = 10^{-3}$, is prescribed here. One Newton iteration suffices at each time step to keep corrector error within the same order of magnitude as local time truncation error.

Newton's iteration process is

$$\begin{bmatrix} \dfrac{\partial R_i}{\partial \alpha_m} & \vdots & \dfrac{\partial R_i}{\partial \beta_k} \\ \cdots\cdots & \vdots & \cdots\cdots \\ \dfrac{\partial R_j^*}{\partial \alpha_m} & \vdots & \dfrac{\partial R_j^*}{\partial \beta_k} \end{bmatrix} \begin{bmatrix} \Delta\alpha_m \\ \cdots \\ \Delta\beta_k \end{bmatrix} = -\begin{bmatrix} R_i \\ \cdots \\ R_j^* \end{bmatrix}. \tag{46}$$

The submatrices of residual sensitivies in the Jacobian or "stiffness" matrix are derived from the Galerkin weighted residuals, Eqs. (39)–(40):

$$\begin{aligned}\frac{\partial R_i}{\partial \beta_k} &= \theta_\xi \int_0^1\int_0^1 \psi_\eta^i \psi_\eta^k \frac{r^2}{r_\eta}\sin\theta\, d\xi\, d\eta\\ &\quad + \frac{1}{\theta_\xi}\int_0^1\int_0^1 \left(\psi_\xi^i - \frac{r_\xi}{r_\eta}\psi_\eta^i\right)\left(\psi_\xi^k - \frac{r_\xi}{r_\eta}\psi_\eta^k\right) r_\eta \sin\theta\, d\xi\, d\eta,\\ &\quad i = 1, \ldots, N,\ k = 1, \ldots, N,\end{aligned} \tag{47}$$

$$\frac{\partial R_j^*}{\partial \beta_k} = \theta_\xi \int_0^1 \left[\frac{c_1}{\Delta t_p} \psi^k - \mathring{f} \frac{\psi_\eta^k}{r_\eta} + \frac{\phi_\eta}{r_\eta^2} \psi_\eta^k \right.$$
$$\left. + \frac{1}{\theta_\xi^2 f^2} \left(\phi_\xi - \frac{r_\xi}{r_\eta} \phi_\eta \right) \left(\psi_\xi^k - \frac{r_\xi}{r_\eta} \psi_\eta^k \right) \right] \psi^j f^2 \sin\theta \, d\xi,$$
$$j = 1, \ldots, N_B, \; k = 1, \ldots, N, \tag{48}$$

$$\frac{\partial R_i}{\partial \alpha_m} = \int_0^1 \int_0^1 \left\{ \left[2 \frac{\partial r}{\partial \alpha_m} - \frac{r}{r_\eta} \frac{\partial r_\eta}{\partial \alpha_m} \right] \theta_\xi \phi_\eta \psi_\eta^i \frac{r}{r_\eta} \right.$$
$$+ \frac{1}{\theta_\xi} \frac{\partial r_\eta}{\partial \alpha_m} \left(\phi_\xi - \frac{r_\xi}{r_\eta} \phi_\eta \right) \left(\psi_\xi^i - \frac{r_\xi}{r_\eta} \psi_\eta^i \right)$$
$$\left. - \frac{r_\eta}{\theta_\xi} \frac{\partial}{\partial \alpha_m} \left(\frac{r_\xi}{r_\eta} \right) \left[\phi_\eta \left(\psi_\xi^i - \frac{r_\xi}{r_\eta} \psi_\eta^i \right) + \psi_\eta^i \left(\phi_\xi - \frac{r_\xi}{r_\eta} \phi_\eta \right) \right] \right\} \sin\theta \, d\xi \, d\eta$$
$$+ \theta_\xi \int_0^1 \left(\frac{c_1}{\Delta t_p} f + 2\mathring{f} \right) f \psi^i \psi^m \sin\theta \, d\xi, \qquad i = 1, \ldots, N, \; m = 1, \ldots, N_B, \tag{49}$$

$$\frac{\partial R_j^*}{\partial \alpha_m} = \theta_\xi \int_0^1 \left\{ - \left[\frac{\phi_\eta^2}{r_\eta^3} \frac{\partial r_\eta}{\partial \alpha_m} + \frac{\psi^m}{\theta_\xi^2 f^3} \left(\phi_\xi - \frac{r_\xi}{r_\eta} \phi_\eta \right)^2 \right.$$
$$\left. + \frac{\phi_\eta}{\theta_\xi^2 f^2} \left(\phi_\xi - \frac{r_\xi}{r_\eta} \phi_\eta \right) \frac{\partial}{\alpha_m} \left(\frac{r_\xi}{r_\eta} \right) \right] + \left[\mathring{f} \frac{\phi_\eta}{r_\eta^2} \frac{\partial r_\eta}{\partial \alpha_m} - \frac{c_1}{\Delta t_p} \frac{\phi_\eta}{r_\eta} \psi^m \right]$$
$$+ \frac{2\psi^m}{f} \left[\mathring{\phi} - \mathring{f} \frac{\phi_\eta}{r_\eta} + \frac{1}{2} \left(\frac{\phi_\eta}{r_\eta} \right)^2 \right.$$
$$\left. + \frac{1}{2} \frac{1}{\theta_\xi^2 f^2} \left(\phi_\xi - \frac{r_\xi}{r_\eta} \phi_\eta \right)^2 \right] \Bigg\} \psi^j f^2 \sin\theta \, d\xi$$
$$+ \frac{1}{8} \int_0^1 \left\{ (f_\xi \psi^m + f \psi_\xi^m) \psi_\xi^j + 2\psi^j (2\theta_\xi^2 f \psi^m + f_\xi \psi_\xi^m) \right.$$
$$\left. - \frac{[\theta_\xi^2 f \psi^m + f_\xi \psi_\xi^m][f f_\xi \psi_\xi^j + \psi^j (2\theta_\xi^2 f^2 + f_\xi^2)]}{\theta_\xi^2 f^2 + f_\xi^2} \right\} \frac{\sin\theta \, d\xi}{(\theta_\xi^2 f^2 + f_\xi^2)^{1/2}},$$
$$j = 1, \ldots, N_B, \qquad m = 1, \ldots, N_B. \tag{50}$$

Equation (46) was solved on the Cray-1B computer at the University of Minnesota with Hood's [38] frontal solver, as modified and improved by Silliman [39], Walters [40], Kheshgi and Scriven [22], and Coyle [41].

The present method is superior to Frederiksen and Watts' [42] application of the space-time finite element method [43] to free surface flow problems. Finite element discretization in time increases the dimension of basis functions by one and frontwidth (or bandwidth) by an order of magnitude. The space-time finite element method would make computation of three-dimensional flows unreasonably

expensive in comparison to other methods. Moreover, conversion of the initial value problem to a boundary value problem requires the restriction that the solution be periodic—compare the perturbation analysis of Tsamopoulos and Brown [6]. Furthermore, Frederiksen and Watt [42] failed to take advantage of the surface divergence theorem, Eq. (22). Instead, they compute the local mean curvature of the free surface by means of second-order finite differences, which was inconsistent with the class of C^0 basis functions they used.

5. Results: Shapes, Pressures, Energies, Frequencies

The dynamic response of an axisymmetric inviscid drop to two classes of disturbances is considered. The first, harmonic velocity potential disturbances of an undeformed drop,

$$\begin{aligned} f(\theta, 0) &= 1, \\ \phi(r, \theta, 0) &= \sum_{n=2}^{\infty} \phi_n r^n P_n(\theta), \qquad \phi_n \geqslant 0,\ n = 2, 3, \ldots, \end{aligned} \tag{51}$$

can arise from a pressure impulse p' of duration δt, because [44]

$$\phi(\mathbf{x}, \delta t) = -\int_0^{\delta t} p'(\mathbf{x}, t)\, dt. \tag{52}$$

Equation (52) is of course dimensionless, and the pressure impulse is measured in units of $\rho v_{\min}^2 R^2$. The second class consists of drops released from static deformation,

$$\begin{aligned} f(\theta, 0) &= 1 + \sum_{n=2}^{\infty} f_n P_n(\theta), \qquad f_n \geqslant 0,\ n = 2, 3, \ldots, \\ \phi(r, \theta, 0) &= 0. \end{aligned} \tag{53}$$

Harmonic disturbances of large n are not used here because a finite basis set is incapable of representing them accurately.

Velocity potential disturbances (51) chosen for the results to follow include: (a) initial second harmonic, $\phi_2 = 0.3$; (b) mixture of initial second and third harmonics, $\phi_2 = \phi_3 = 0.1$; (c) initial third harmonic, $\phi_3 = 0.18$; (d) initial fourth harmonic, $\phi_4 = 0.18$. Disturbance amplitudes ϕ_n given here must be multiplied by $\sqrt{8}$ for comparison to Tsampoulos and Brown [6] and others, because $v_{\min}$ is used here as a unit of measurement. A tesselation of 4×12 biquadratic elements was used in all cases except (b). In case (b) a 4×10 tessellation of biquadratic elements was used.

Sequences of drop shapes resulting from velocity potential disturbances (a)–(d) are shown in Fig. 5. The dynamic response to case (a), $\phi_2 = 0.3$, has a ratio of major

(L) to minor (W) axes at maximum prolate deformation of $L/W = 2.64$. In Fig. 6 a sequence of two-lobed drop shapes is shown, beginning with a static deformation of $f_2 = 0.5$, or $L/W = 2.0$. The sequences of shapes in Figs. 5 and 6 show signs of higher harmonics. In the sequence which is initially fourth harmonic, Fig. 5(d), some sixth harmonic is visible in the drop shape at $t = 2.119$ and even some eighth harmonic in the drop shapes at $t = 6.119$ and $t = 6.586$. Some fourth harmonic is

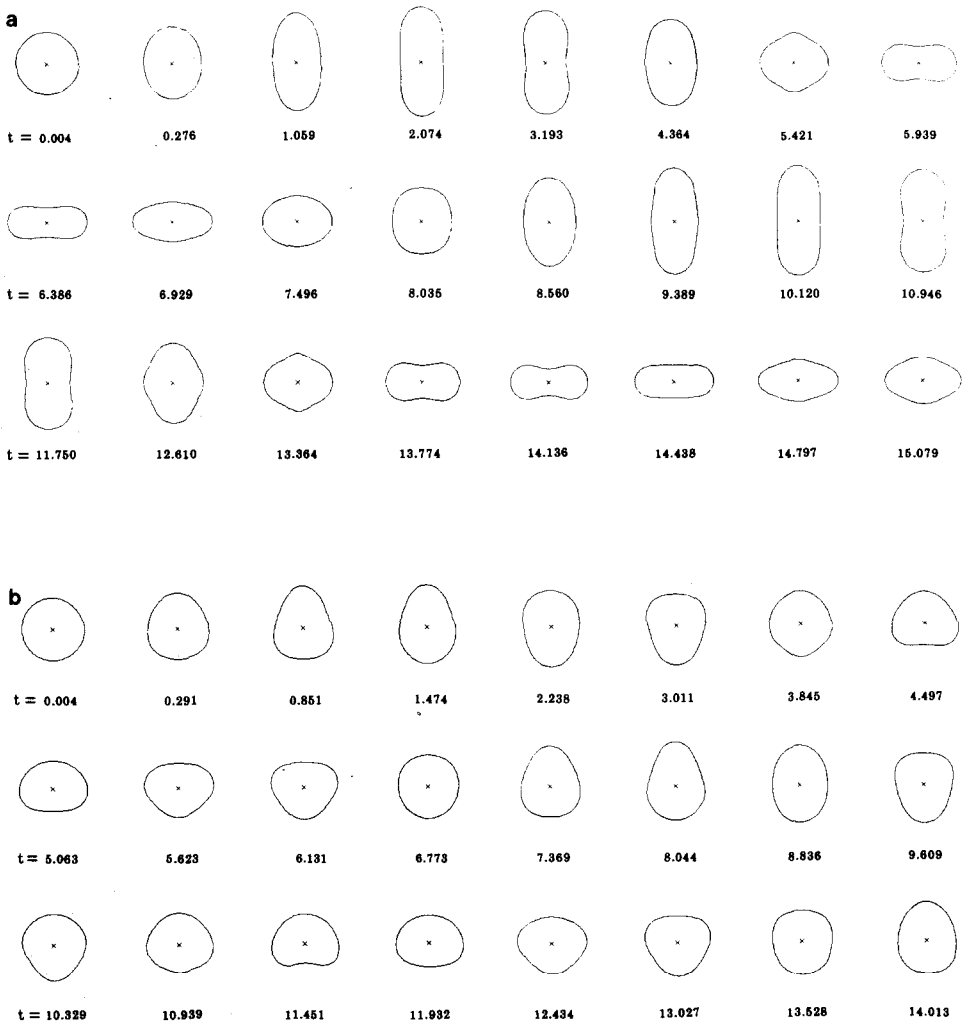

FIG. 5. Sequences of drop shapes: initial velocity potential disturbance. Shapes are shown at every fourth time step in Figs. 5(a–d) and 6. The time t is listed beneath each drop shape, because the time step is chosen adaptively: (a) $\phi_2 = 0.3$; (b) $\phi_2 = \phi_3 = 0.1$; (c) $\phi_3 = 0.18$; (d) $\phi_4 = 0.18$.

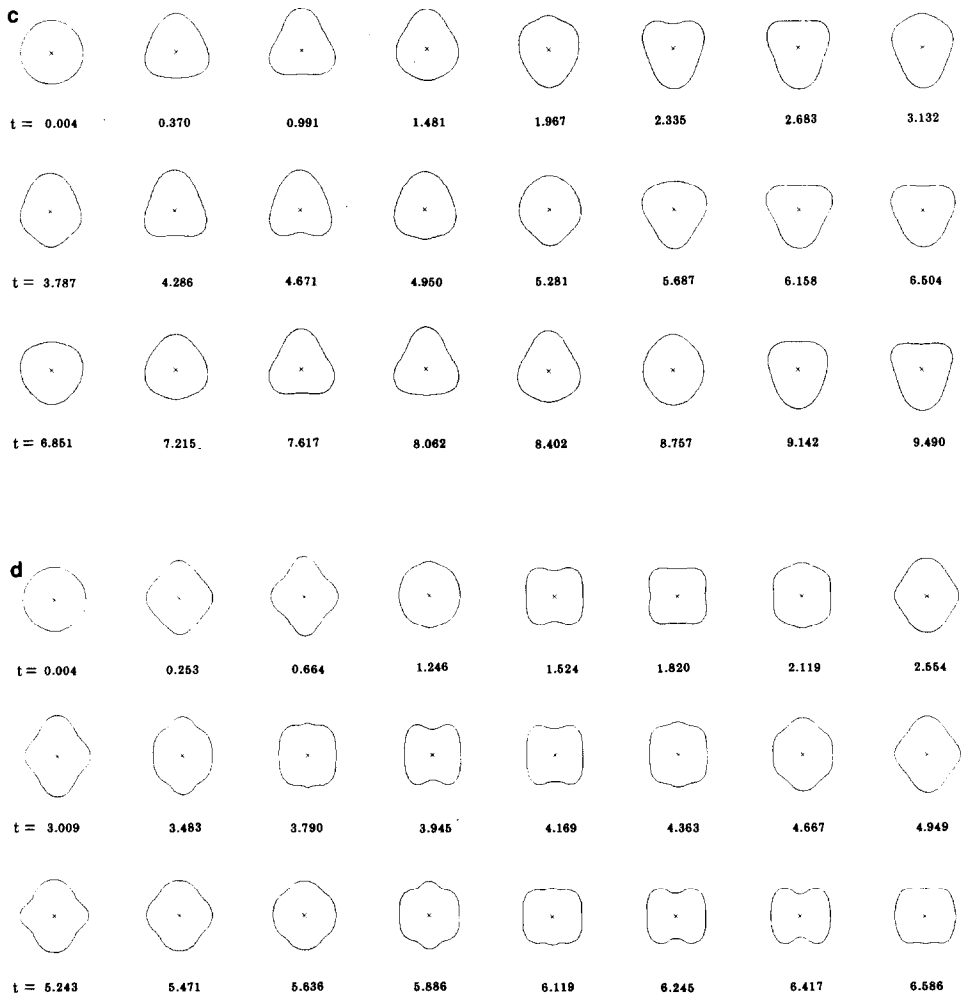

FIG. 5—*Continued*

present in the large amplitude oscillation of initial second harmonic, Fig. 5(a), e.g., in drop shapes at $t = 5.421$, 12.61, and 13.364.

Pressure inside the drop is computed from the velocity potential field and Eq. (4). The complexity of the flow inside the drop is evident in the pressure fields shown in Fig. 7, especially in cases of initial third harmonic—Fig. 7(c)—and initial mixture of second and third harmonics—Fig. 7(b). Pressure fields are calculated when the drop is near its maximum defomation; contours are drawn at even intervals.

Accuracy of the results is attested by virtual constancy of drop volume V and mechanical energy $E_k + E_s$, as well as the smallness of mass flux $I(t)$ and the axial

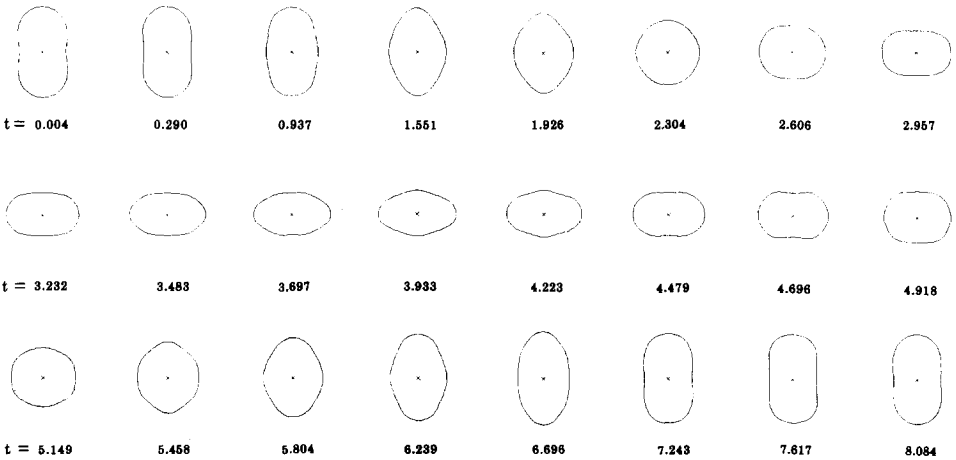

FIG. 6. Sequence of drop shapes: initial static deformation, $f_2 = 0.5$.

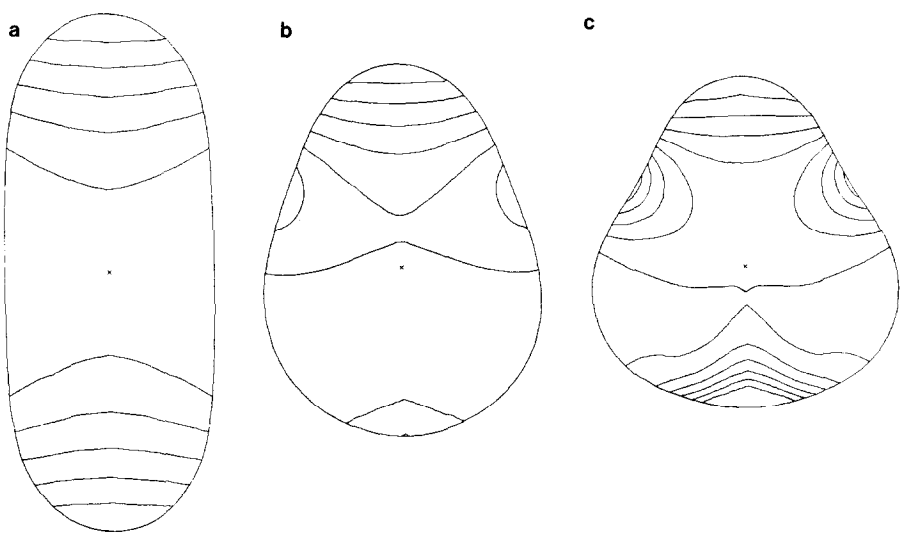

FIG. 7. Pressure fields. Isobars taken at (a) $\phi_2 = 0.3$, $t = 1.829$; (b) $\phi_2 = \phi_3 = 0.1$, $t = 1.31$. (c) $\phi_3 = 0.18$, $t = 1.361$.

component of momentum flux $M_z(t)$ across the drop surface. In dimensionless form,

$$\tilde{V} = \frac{3V}{4\pi R^3} = \frac{1}{2}\int_0^\pi f^3 \sin\theta \, d\theta \tag{54}$$

$$\tilde{I}(t) = I(8\sigma\rho R^3)^{-1/2} = 2\pi \int_0^\pi \left(\phi_r - \frac{f_\theta}{f^2}\phi_\theta - \mathring{f}\right) f^2 \sin\theta \, d\theta \tag{55}$$

$$\tilde{M}_z(t) = \frac{M_z}{8\sigma R} = 2\pi \int_0^\pi \left(\phi_r \cos\theta - \frac{\phi_\theta}{f}\sin\theta\right)\left(\phi_r - \frac{f_\theta}{f^2}\phi_\theta - \mathring{f}\right) f^2 \sin\theta \, d\theta \tag{56}$$

$$\tilde{E}_k(t) = \frac{E_k}{8\sigma R^2} = \pi \int_0^\pi \int_0^f \left[\phi_r^2 + \left(\frac{\phi_\theta}{r}\right)^2\right] r^2 \sin\theta \, dr \, d\theta \tag{57}$$

$$\tilde{E}_s(t) = \frac{E_s}{8\sigma R^2} = \frac{\pi}{4}\int_0^\pi (f^2 + f_\theta^2)^{1/2} f \sin\theta \, d\theta \tag{58}$$

$$\frac{\tilde{E}_k(t) + \tilde{E}_s(t)}{\tilde{E}_k(0) + \tilde{E}_s(0)} = 1. \tag{59}$$

Here $\tilde{E}_k$ and $\tilde{E}_s$ are kinetic and surface energies, respectively. Hereafter, tildes are again suppressed. As shown in Fig. 8, mechanical energy is conserved to within 0.2–0.5%. Fluctuations in drop volume and the mass and axial momentum fluxes across the interface are all of order ε, the local time truncation error, when $\varepsilon = 10^{-3}$.

Kinetic and surface energy should, to first-order in disturbance amplitude, vary as $\sin^2 t$ or $\cos^2 t$ [6]. This is verified in Fig. 9 for moderate amplitude oscillations started by a velocity potential disturbance. When oscillations are of moderate amplitude, kinetic energy returns periodically to zero (static deformation), but surface energy no longer returns to the reference level of $\pi/2$, because the drop never returns to its initial spherical shape.

Surface and kinetic energies of moderate and large amplitude oscillations are plotted in Fig. 10. The response to an initial mixture of second and third harmonics is quasiperiodic, i.e., governed by two or more frequencies of oscillation that are not integer multiples of each other. Dynamic response to third- or fourth-harmonic disturbances is also quasiperiodic. An initially pure mode of oscillation of moderate or large amplitude can cause mode coupling, i.e., excitation of other modes of oscillation. Quasiperiodicity is one consequence of mode coupling which is **excluded** in the perturbation analysis of Tsamopoulos and Brown [6].

Mode coupling is analyzed here by Fourier spectral analysis of the motion of a particle on the drop surface at a pole, $f(0, t)$. Particle path lines at the pole $\theta = 0$ and their Fourier power spectra are shown in Fig. 11. Frequencies are measured in units of $\nu_{\min}$. Thus $\nu_0 = 1$ for pure second-harmonic, $\nu_0 = 1.936$ for pure third-harmonic, and $\nu_0 = 3$ for pure fourth-hamonic oscillations. The minimum frequency resolution is half the spacing between frequencies shown, or 5–15% in the cases

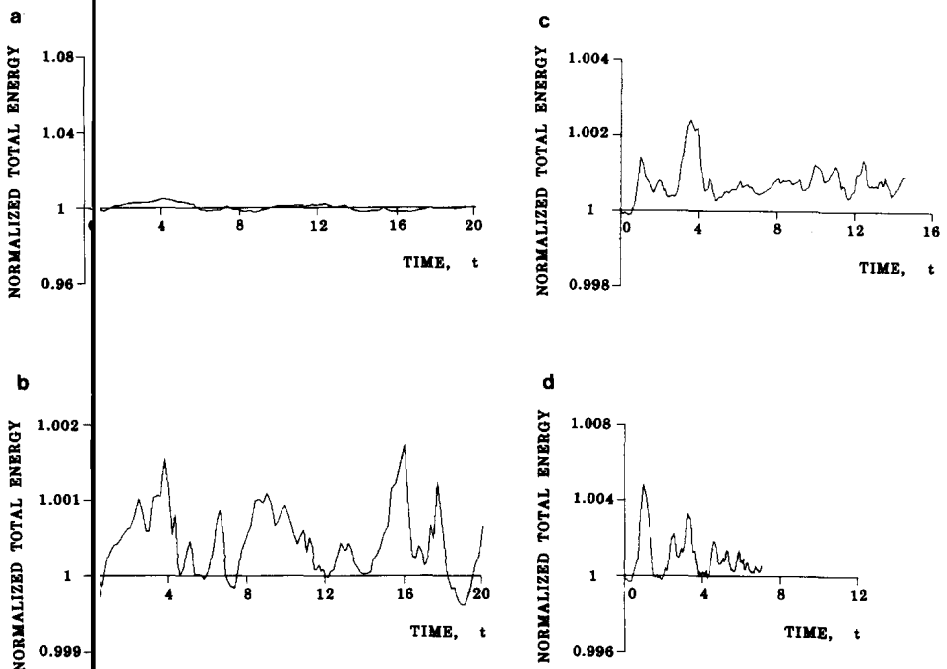

FIG. 8. Normalized total energy: (a) $\phi_2 = 0.3$; (b) $\phi_2 = \phi_3 = 0.1$; (c) $\phi_3 = 0.18$; (d) $\phi_4 = 0.18$.

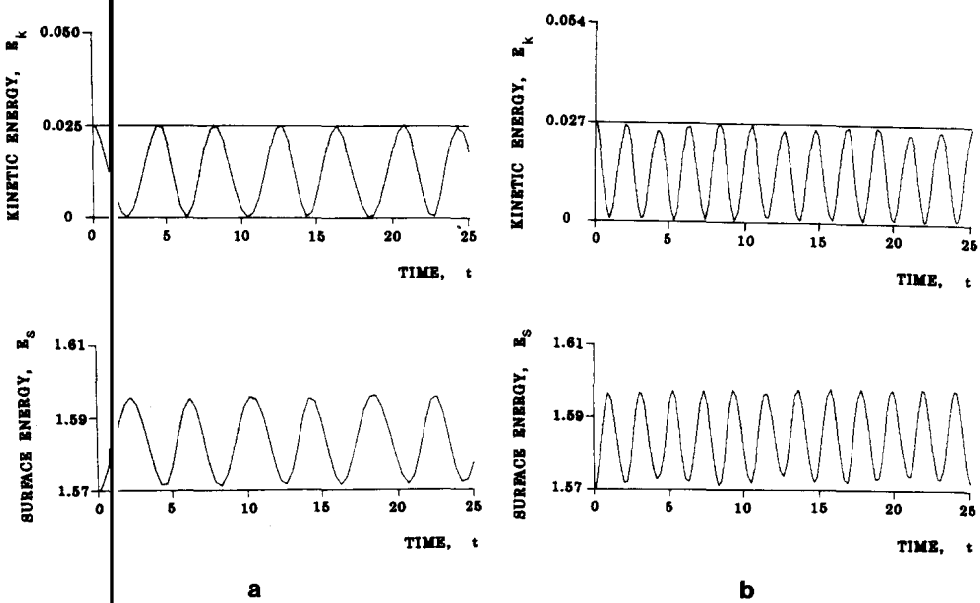

FIG. 9. Kinetic and surface energy: moderate amplitude oscillations: (a) $\phi_2 = 0.1$; (b) $\phi_3 = 0.1$.

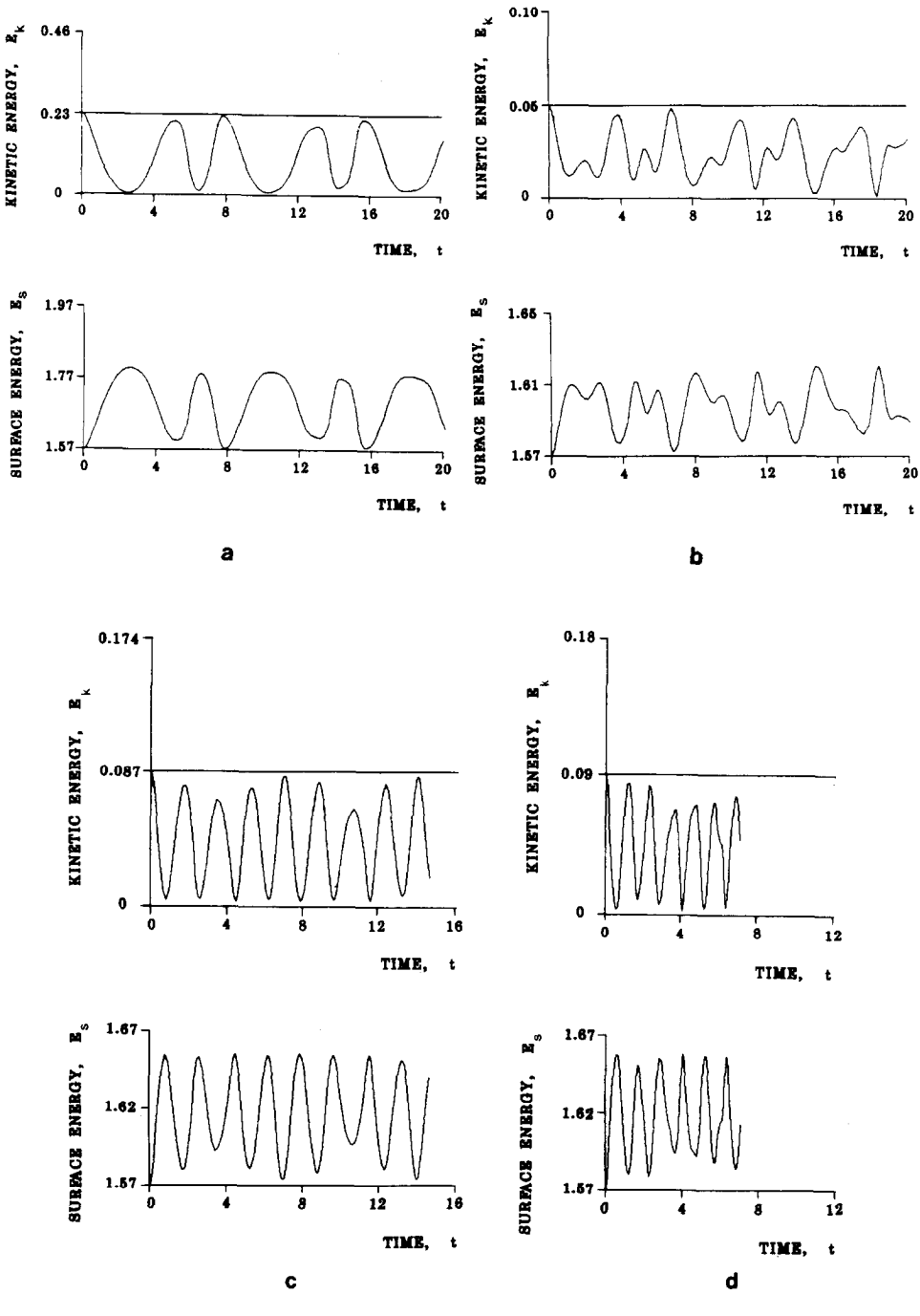

FIG. 10. Kinetic and surface energy: (a) $\phi_2 = 0.3$; (b) $\phi_2 = \phi_3 = 0.1$; (c) $\phi_3 = 0.18$; (d) $\phi_4 = 0.18$.

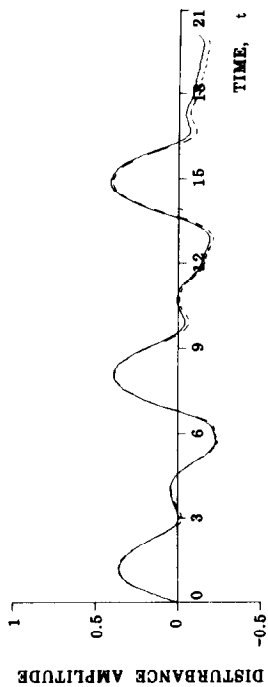
DISTURBANCE AMPLITUDE
TIME, t
1
0.5
0
-0.5
0
3
6
9
12
15
18
21

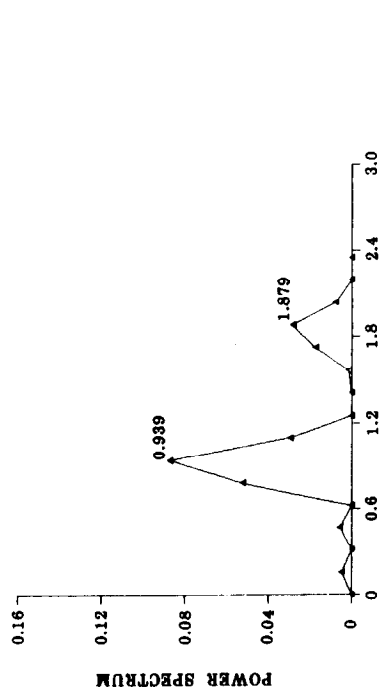
POWER SPECTRUM
FREQUENCY, ω
0.16
0.12
0.08
0.04
0
0.6
1.2
1.8
2.4
3.0
0.939
1.879

b

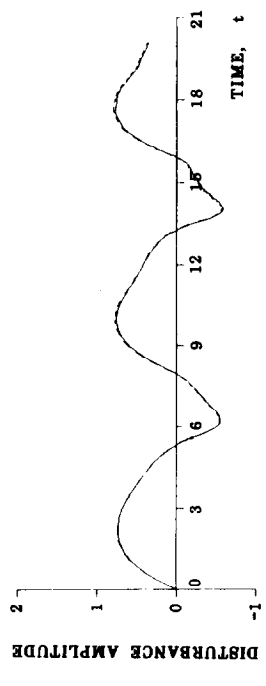
DISTURBANCE AMPLITUDE
TIME, t
2
1
0
-1
0
3
6
9
12
15
18
21

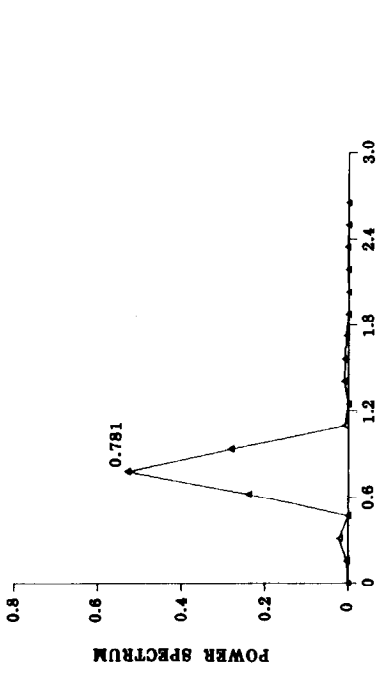
POWER SPECTRUM
FREQUENCY, ω
0.8
0.6
0.4
0.2
0
0.6
1.2
1.8
2.4
3.0
0.781

a

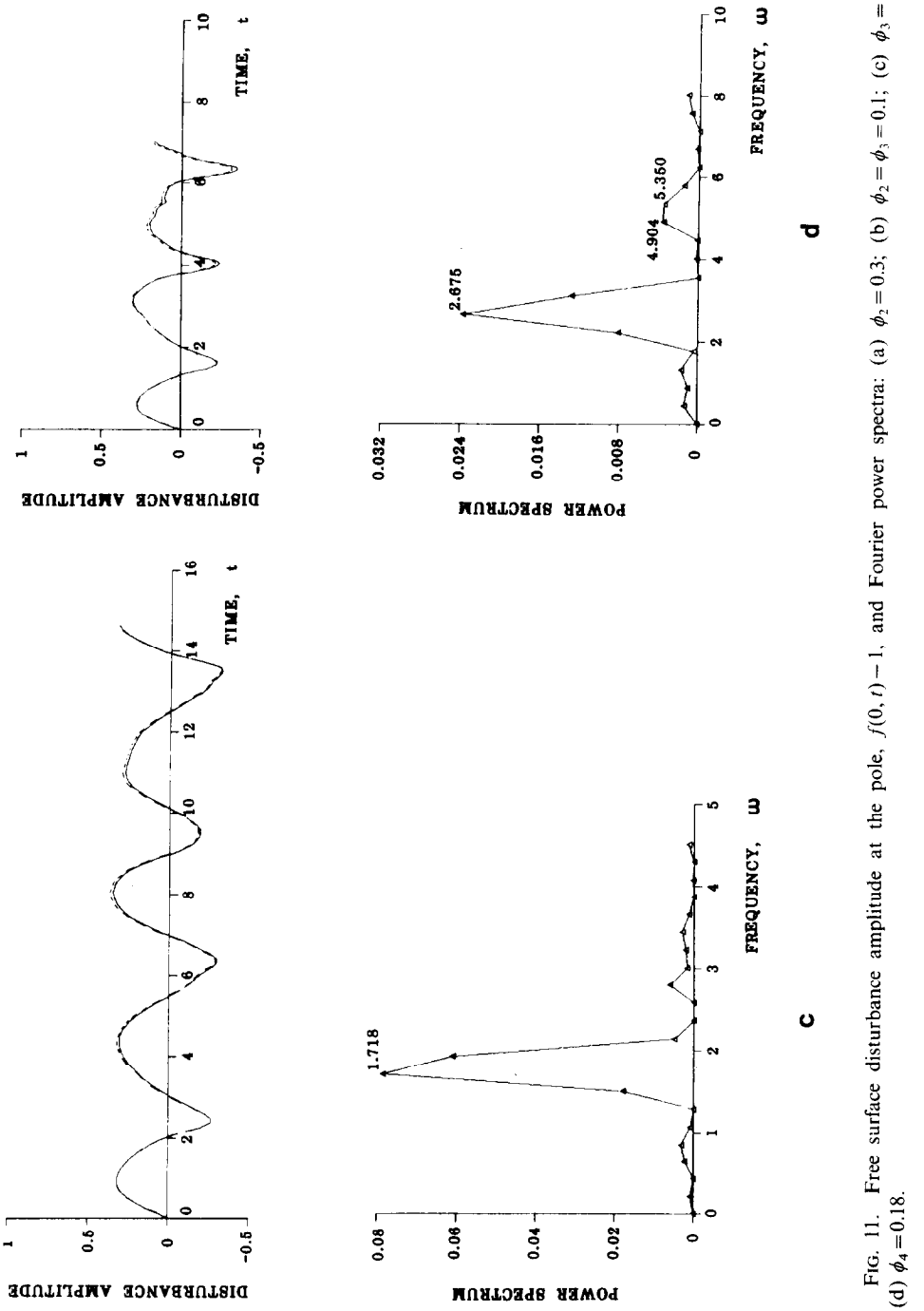

FIG. 11. Free surface disturbance amplitude at the pole, $f(0,t)-1$, and Fourier power spectra: (a) $\phi_2=0.3$; (b) $\phi_2=\phi_3=0.1$; (c) $\phi_3=0.18$; (d) $\phi_4=0.18$.

shown. In Fig. 11 the large amplitude response to an initially second-harmonic disturbance, $\phi_2 = 0.3$, is dominated by a second-harmonic mode of frequency $\nu \approx 0.78$, which amounts to a 22% decrease in frequency. Dynamic response to higher harmonics displays not only frequency shift but also secondary frequencies, e.g., the third harmonic couples to the second, fourth, and sixth harmonics and the fourth harmonic couples to the second, sixth, and eighth. These couplings are also predicted by Tsamopoulos and Brown's [6] perturbation analysis of frequency shift.

Particle path lines are also calculated from the velocity potential field,

$$\mathbf{x}(f, 0, t) = \mathbf{x}(f, 0, 0) + \int_0^t \nabla\phi(f, 0, t)\, dt. \tag{60}$$

Comparison of $\mathbf{x}(f, 0, t)$ from Eq. (60) to $f(0, t)$ gives an estimate of the accumulation of local time truncation error. These meaures of amplitude at the pole are in good agreement—see Fig. 11—except for the case of mixed initial second- and third-harmonics with a tessellation of 4×10 elements. Increasing the size of the basis to 4×12 elements gives sufficient accuracy in $\nabla\phi$ to eliminate the visible deviations in path lines in Fig. 11(b).

Particle path lines, Fig. 11(a), and surface and kinetic energies, Fig. 10(a), show that the second-harmonic oscillation of large-amplitude spends more time in prolate form than in oblate form. Finite element results for shape deformations that are initially second-harmonic are compared to perturbation results, marker-and-cell calculations, and experimental results for percentage of time spent in prolate form, Fig. 12, and the percentage change in frequency, Fig. 13. The results are expressed

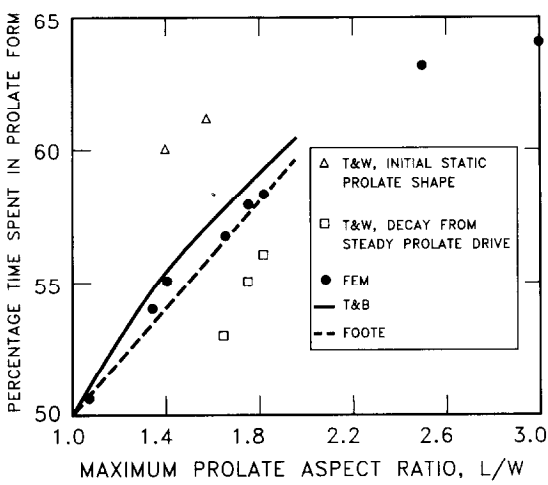

FIG. 12. Percentage of each period of second harmonic oscillation spent in prolate shape vs maximum prolate aspect ratio: (●) finite element analysis; (———) asymptotic analysis of Tsamopoulos and Brown [6] (cf. Fig. 4 in [6]); (--) marker-and-cell calculations of Foote [9]; experimental results of Trinh and Wang [8] (□) for decay from steady prolate drive, and (△) for initial static prolate shape. Experimental results shown are for 1-cm^3 ($R = 0.62$ cm) drops.

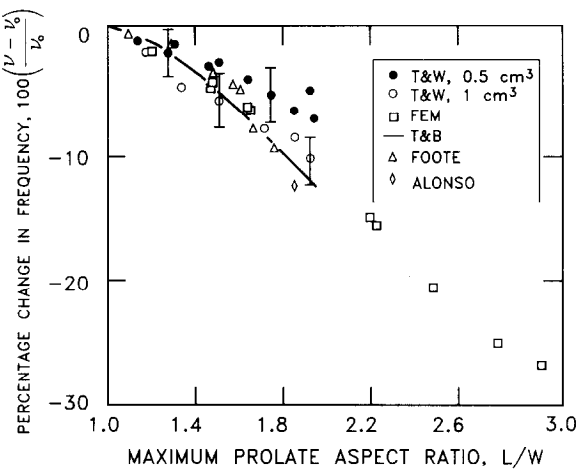

FIG. 13. Percentage change in frequency of second harmonic oscillation vs maximum prolate aspect ratio: (□) finite element analysis; (———) asymptotic analysis of Tsamopoulos and Brown [6]; marker-and-cell calculations of (△) Foote [9], and (◇) Alonso [10]; experimental results of Trinh and Wang [8] (●) $R = 0.49$ cm, (○) $R = 0.62$ cm. The bars on some of the experimental data points indicate uncertainty in the measurements.

as functions of the maximum prolate aspect ratio, L/W. Drop oscillations of L/W up to three are computed by finite element analysis, as compared to the oscillations of L/W less than two investigated by the previously listed other means. The computed frequency shifts at $L/W = 1.48$ and 1.64 are virtually identical—see Fig. 13—to the asymptotic prediction of Tsamopoulos and Brown [6]. At the same values of L/W the computed times spent in prolate form are within 1% of the asymptotic results. Agreement of calculated frequency shifts and times spent in prolate form with experimental results is good, with two exceptions. First, viscous drops spend less time in prolate form than inviscid drops when released from a steady acoustic drive, but more time in prolate form than inviscid drops when released from an initial static shape (deformation). Second, small drops of silicone oil and carbon tetrachloride in water released from an acoustic drive [8] show systematic deviation from inviscid predictions. Coupling between viscosity and drop oscillation may be the cause of the latter disagreement [6].

6. SUMMARY

The results of this paper are in excellent agreement with Rayleigh's [5] linear analysis for infinitesimal amplitude oscillations and Tsamopoulos and Brown's [6] perturbation results for small and moderate amplitude oscillations of inviscid axisymmetric drops. In constrast to perturbation analyses, the computer-aided method used here adapts easily to analysis of large amplitude oscillations, whether

periodic or quasiperiodic, and admits a variety of initial conditions. Furthermore, the predictions made here also accord with those of Lundgren and Mansour [7], who compared results of some of their simulations made by means of the boundary integral method to a preprint of the present paper.

When an oscillating inviscid liquid drop is placed in an electric or a magnetic field, one must solve the appropriate Maxwell's equations along with the equations solved in this paper. When the fluids involved are so-called linearly polarizable media, the electric or magnetic field distributions can be determined by either the DD or BI methods. However, Boudouvis *et al.* [45] showed that it is necessary to account for the nonlinearity of magnetization with respect to field stength in analyzing the magnetohydrostatic equilibria of ferrofluid drops in external magnetic fields. For such nonlinearly polarizable fluids, the Maxwell equations are nonlinear partial differential equations and cannot be solved by the BI method. Therefore, the approach presented in this paper is not just an alternative to the BI method but is likely to prove indispensable in analyzing the inviscid oscillations of ferrofluid drops or their electric analogs.

Computer-aided analyses of the finite amplitude oscillations of drops and of the breakup of oscillating drops in liquid–liquid systems are still pending (cf. Fig. 3). Analyses of these two liquid problems will require the capabilities of DD methods such as the one presented in this paper.

ACKNOWLEDGMENTS

This research was supported by the NASA Fund for Independent Research, the University of Minnesota Computer Center, and the Office of Basic Energy Sciencies, U.S. Department of Energy under Contract DE-AC05-84OR21400 with Martin Marietta Energy Systems, Inc. One of us, R.E.B., was partially supported by a dissertation fellowship from the University of Minnesota.

REFERENCES

1. O. A. BASARAN, T. C. SCOTT, AND C. H. BYERS, *AIChEJ* **35**, 1263 (1989).
2. J. R. CARRUTHERS, in *Proceedings, International Colloquium on Drops and Bubbles*, edited by D. J. Collins, M. S. Plesset, and M. M. Saffren (Jet Propulsion Laboratory, Pasadena, CA, 1974), Vol. 1, p. 161.
3. J. R. CARRUTHERS AND J. R. TESTARDI, *Annu. Rev. Mater. Sci.* **13**, 247 (1983).
4. P. R. BRAZIER-SMITH, *J. Fluid Mech.* **50**, 417 (1971).
5. LORD RAYLEIGH, *Proc. R. Soc. London* **29**, 71 (1879).
6. J. A. TSAMOPOULOS AND R. A. BROWN, *J. Fluid Mech.* **127**, 519 (1983).
7. T. S. LUNDGREN AND N. N. MANSOUR, *J. Fluid Mech.* **194**, 479 (1988).
8. E. TRINH AND T. G. WANG, *J. Fluid Mech.* **122**, 315 (1982).
9. G. B. FOOTE, *J. Comput. Phys.* **11**, 507 (1973).
10. C. T. ALONSO, in *Proceedings, International Colloquium on Drops and Bubbles*, edited by D. J. Collins, M. S. Plesset, and M. M. Saffren (Jet Propulsion Laboratory, Pasadena, CA, 1974), Vol. 1, p. 139.
11. C. T. ALONSO, J. M. LEBLANC, AND J. R. WILSON, in *Proceedings, Second International Colloquium*

on Drops and Bubbles, edited by D. H. LeCroissette (Jet Propulsion Laboratory, Pasadena, CA, 1982), p. 268.
12. F. H. HARLOW, *Proc. Symp. Appl. Math.* **15**, 269 (1963).
13. F. H. HARLOW, A. A. AMSDEN, AND J. R. NIX, *J. Comput. Phys.* **20**, 119 (1976).
14. J. R. NIX AND D. STROTTMAN, in *Proceedings, Second International Colloquium on Drops and Bubbles*, edited by D. H. LeCroisette (Jet Propulsion Laboratory, Pasadena, CA, 1982), p. 260.
15. P. M. GRESHO, R. L. LEE, AND R. C. SANI, in *Recent Advances in Numerical Methods in Fluids*, edited by C. Taylor and K. Morgan (Pineridge Press, Swansea, UK, 1979), Vol. 1, p. 27.
16. S. A. ORSZAG, *J. Comput. Phys.* **37**, 70 (1980).
17. J. HAPPEL AND H. BRENNER, *Low Reynolds Number Hydrodynamics* (Martinus Nijhoff, Boston, 1973).
18. S. WEINBAUM, P. GANATOS, AND Z. YAN, *Annu. Rev. Fluid Mech.* **22**, 275 (1990).
19. J. BARLOW, *Int. J. Numer. Methods Eng.* **10**, 243 (1976).
20. H. SAITO AND L. E. SCRIVEN, *J. Comput. Phys.* **42**, 53 (1981).
21. S. F. KISTLER AND L. E. SCRIVEN, in *Computational Analysis of Polymer Processing*, edited by J. R. A. Pearson and S. M. Richardson (Applied Science, London, 1983).
22. H. S. KHESHGI AND L. E. SCRIVEN, in *Finite Elements in Fluids*, edited by J. T. Oden *et al.* (Wiley, New York, 1983), Vol. 5.
23. M. S. LONGUET-HIGGINS AND E. D. COKELET, *Proc. R. Soc. London A* **350**, 1 (1976).
24. G. R. BAKER, D. I. MEIRON, AND S. A. ORSZAG, *J. Fluid Mech.* **123**, 477 (1982).
25. G. R. BAKER, D. I. MEIRON, AND S. A. ORSZAG, *Phys. Fluids* **23**, 1485 (1980).
26. E. C. HUME, III, R. A. BROWN, AND W. M. DEEN, *Int. J. Numer. Methods Eng.* **21**, 1295 (1985).
27. R. E. BENNER, Ph.D. thesis, University of Minnesota, Minneapolis, 1983 (unpublished). Available from University Microfilms, Inc., Ann Arbor, MI.
28. R. E. BENNER, T. W. PATZEK, O. A. BASARAN, AND L. E. SCRIVEN, *J. Fluid Mech.*, submitted.
29. O. A. BASARAN, Ph.D. thesis, University of Minnesota, 1984 (unpublished). Available from University Microfilms, Inc., Ann Arbor, MI.
30. O. A. BASARAN, T. W. PATZEK, R. E. BENNER, AND L. E. SCRIVEN, *J. Fluid Mech.*, submitted.
31. C. A. MILLER AND L. E. SCRIVEN, *J. Fluid Mech.* **32**, 417 (1968).
32. C. E. WEATHERBURN, *Differential Geometry of Three Dimensions* (Cambridge Univ. Press, Cambridge, UK, 1927).
33. H. LAMB, *Hydrodynamics* (Dover, New York, 1932).
34. W. H. REID, *Q. Appl. Math.* **18**, 86 (1960).
35. R. ARIS, *Vectors, Tensors, and the Basic Equations of Fluid Mechanics* (Prentice-Hall, Englewood Cliffs, NJ, 1962).
36. G. STRANG AND G. J. FIX, *An Analysis of the Finite Element Method* (Prentice-Hall, Englewood Cliffs, NJ, 1973).
37. M. LUSKIN AND R. RANNACHER, *Appl. Anal.* **14**, 117 (1982).
38. P. HOOD, *Int. J. Numer. Methods Eng.* **10**, 379 (1976); Correction, *Int. J. Numer. Methods Eng.* **11**, 1055 (1977).
39. W. J. SILLIMAN, Ph.D. thesis, University of Minnesota, 1979 (unpublished). Available from University Microfilms, Inc., Ann Arbor, MI.
40. R. A. WALTERS, *Comput. Fluids* **8**, 265 (1980).
41. D. J. COYLE, "The Fluid Mechanics of Roll Coating: Steady Flows, Stability, and Rheology," Ph.D. Thesis, University of Minnesota, 1984 (unpublished). Available from University Microfilms, Inc., Ann Arbor, MI.
42. C. S. FREDERICKSEN AND A. M. WATTS, *J. Comput. Phys.* **39**, 282 (1981).
43. R. BONNEROT AND P. JAMET, *J. Comput. Phys.* **25**, 163 (1977).
44. G. K. BATCHELOR, *An Introduction to Fluid Dynamics* (Cambridge Univ. Press, Cambridge, UK, 1967).
45. A. G. BOUDOUVIS, J. L. PUCHALLA, AND L. E. SCRIVEN, *Chem. Eng. Commun.* **67**, 129 (1988).